

# Linköping University Post Print

## **Appropriation of the MinD protein-interaction motif by the dimeric interface of the bacterial cell division regulator MinE**

Houman Ghasriani, Thierry Ducat, Chris T Hart, Fatima Hafizi, Nina Chang, Ali Al-Baldawi, Saud H Ayed, Patrik Lundström, Jo-Anne R Dillon and Natalie K Goto

N.B.: When citing this work, cite the original article.

Original Publication:

Houman Ghasriani, Thierry Ducat, Chris T Hart, Fatima Hafizi, Nina Chang, Ali Al-Baldawi, Saud H Ayed, Patrik Lundström, Jo-Anne R Dillon and Natalie K Goto, Appropriation of the MinD protein-interaction motif by the dimeric interface of the bacterial cell division regulator MinE, 2010, PROCEEDINGS OF THE NATIONAL ACADEMY OF SCIENCES OF THE UNITED STATES OF AMERICA, (107), 43, 18416-18421.

<http://dx.doi.org/10.1073/pnas.1007141107>

Copyright: National Academy of Sciences; 1999

<http://www.nas.edu/>

Postprint available at: Linköping University Electronic Press

<http://urn.kb.se/resolve?urn=urn:nbn:se:liu:diva-62726>

**Appropriation of the MinD protein-interaction motif by the dimeric interface of the bacterial cell division regulator MinE.**

*Houman Ghasriani<sup>a</sup>, Thierry Ducat<sup>a</sup>, Chris T. Hart<sup>a</sup>, Fatima Hafizi<sup>b</sup>, Nina Chang<sup>b</sup>, Ali Al-Baldawi<sup>b</sup>, Saud H. Ayed<sup>b</sup>, Patrik Lundström<sup>c</sup>, Jo-Anne R. Dillon<sup>d</sup> and Natalie K. Goto<sup>a,b,\*</sup>*

Department of Chemistry<sup>a</sup> and Department of Biochemistry, Microbiology and Immunology, University of Ottawa, Ontario, Canada, K1N 6N5<sup>b</sup>; Division of Molecular Biotechnology, Department of Physics, Chemistry and Biology, Linköping University, Linköping, Sweden, SE-58183<sup>c</sup>; Department of Microbiology and Immunology, Vaccine and Infectious Disease Organization, Department of Biology, University of Saskatchewan, 120 Veterinary Road, Saskatoon, Saskatchewan S7N 5E3<sup>d</sup>

***\*Corresponding author:***

Natalie K. Goto

Department of Chemistry, University of Ottawa, 10 Marie Curie, Ottawa, ON, K1N 6N5  
Canada

Tel: (613) 562-5800 ext. 6918

Fax: (613) 562-5170

Email: [ngoto@uottawa.ca](mailto:ngoto@uottawa.ca)

***Classification:*** Biological Sciences, Biochemistry

***Data Deposition:*** Atomic coordinates and NMR restraint files have been deposited in the Protein Data Bank, [www.pdb.org](http://www.pdb.org) (PDB ID code 2KXO).

## Abstract

MinE is required for the dynamic oscillation of Min proteins that restricts formation of the cytokinetic septum to the midpoint of the cell in gram negative bacteria. Critical for this oscillation is MinD-binding by MinE to stimulate MinD ATP hydrolysis, a function that had been assigned to the first ~30 residues in MinE. Previous models based on the structure of an autonomously folded dimeric C-terminal fragment suggested that the N-terminal domain is freely accessible for interactions with MinD. We report here the solution NMR structure of the full-length MinE dimer from *Neisseria gonorrhoeae*, with two parts of the N-terminal domain forming an integral part of the dimerization interface. Unexpectedly, solvent accessibility is highly restricted for residues that were previously hypothesized to directly interact with MinD. To delineate the true MinD-binding region, in vitro assays for MinE-stimulated MinD activity were performed. The relative MinD binding affinities obtained for full-length and N-terminal peptides from MinE demonstrated that residues that are completely buried in the dimeric interface nonetheless participate in direct interactions with MinD. According to results from NMR spin relaxation experiments, access to these buried residues may be facilitated by the presence of conformational exchange. We suggest that this concealment of MinD-binding residues by the MinE dimeric interface provides a mechanism for prevention of non-specific interactions, particularly with the lipid membrane, to allow the free diffusion of MinE that is critical for Min protein oscillation.

\body

## **Introduction**

The dynamic three-dimensional subcellular organization of proteins in bacteria is emerging as an important mechanism for the regulation of many critical processes. The bacterial MinD and MinE proteins are a well-characterized example of this type of system, oscillating in a controlled manner from pole-to-pole to localize MinC such that cell division at non-productive polar sites is prevented (1-4). Underlying this oscillation is a dynamic polymeric superstructure formed by MinD that extends out from the cell pole as a helical coil (5, 6). MinE preferentially localizes to the leading edge of this coil to form a concentrated annulus of MinE (Fig. 1A). This structure, known as the E-ring, drives the ordered disassembly of the polymeric structure from the mid-cell back to the pole (7, 8). Concomitant establishment of a new Min polymer at the opposite cell pole initiates another cycle of growth and disassembly.

The energy for Min protein oscillation is provided by the MinD-catalyzed hydrolysis of ATP (9), in a reaction cycle that is stimulated by MinE (Fig. 1B). The region of MinE thought to be responsible for this stimulation of MinD ATPase activity is known as the anti-MinCD domain and encompasses the first ~30 residues of its amino acid sequence (10). A truncated MinE sample containing the remaining C-terminal residues (31-88 in the *Escherichia coli* protein), also known as the topological specificity domain (TSD), has been shown to adopt an autonomous fold as a dimeric  $\alpha\beta$  sandwich (11, 12). The TSD can interfere with the topologically specific activity of the full-length protein, since its overexpression in a wild-type (WT) background gives rise to products of polar cell division known as minicells (13-15).

Current models of MinE activity are based on the TSD structure and the observation that a peptide comprised of the first 22 residues of MinE is largely unstructured, with some propensity to sample helical conformations (12, 16). According to this model, the anti-MinCD domain is largely unfolded and solvent-exposed, allowing free interactions with membrane-bound MinD. However, we have shown that in the full-length MinE protein from *Neisseria gonorrhoeae* (Ng) the anti-MinCD domain is stably folded, with interactions involving the topological specificity domain (17).

Since the presence of structure in this part of the protein could significantly change current models of MinD-MinE interactions, we set out to determine the structure of a full-length MinE protein by solution NMR. This structure reveals an integral part of the dimeric interface in full-length MinE being formed by two regions of the anti-MinCD domain. We show using assays based on in vitro stimulation of MinD activity that residues located at solvent-inaccessible sites in the dimeric interface of this structure nonetheless play a direct role in binding to MinD. This sequestration of a protein-binding motif away from the aqueous environment helps to explain how MinE can minimize non-specific interactions, an event that would significantly affect Min protein oscillation.

## **Results**

### ***Ng-MinE structure***

Using standard heteronuclear solution NMR techniques, an ensemble of structures was determined for a full-length Ng-MinE sample. This was done using the E46A mutant, since it exhibited more favorable solubility characteristics than the wild-type protein, and retained structural characteristics that were highly similar to that of WT as

determined by circular dichroism and backbone NMR secondary chemical shifts (17, 18). As shown in Figure 2, E46A Ng-MinE forms a homodimer, with each subunit being comprised of a 3-strand  $\beta$ -sheet packed against an  $\alpha$ -helix ( $\alpha$ B, residues 39 to 54) in an approximately parallel orientation. Flanking the other side of the  $\beta$ -sheet is a shorter N-terminal  $\alpha$ -helix from the other subunit in the dimer ( $\alpha$ A, residues 3 to 8), which is roughly perpendicular with respect to the sheet.

An extensive homodimeric interface supported by intermolecular NOEs is formed by inter-subunit backbone hydrogen bonding between  $\beta$ 1 strands, and interactions involving hydrophobic side chains from these strands (Leu<sup>22</sup>, Ile<sup>24</sup>, Ile<sup>26</sup>), while side chains from the two  $\alpha$ B helices (Tyr<sup>39</sup>, Thr<sup>42</sup>, Leu<sup>43</sup>, Ala<sup>46</sup>, Val<sup>50</sup>, Tyr<sup>54</sup>, Val<sup>55</sup>) also contribute to the dimeric interface (Fig. 2B). This part of the interface buries a total of 1200 Å<sup>2</sup> surface area per subunit. In addition, intermolecular NOEs involving the N-terminal  $\alpha$ A helix were also assigned showing interactions with the  $\beta$ -sheet (Fig. S1). The resulting structure shows that ~300 Å<sup>2</sup>/subunit of the  $\beta$ -sheet is buried by this part of the intermolecular interaction, with Ile<sup>4</sup>, Leu<sup>7</sup> and Phe<sup>8</sup> from  $\alpha$ A making specific inter-subunit contacts with a conserved hydrophobic patch formed by residues, Ile<sup>25</sup>, Ala<sup>27</sup>, Met<sup>72</sup> and Val<sup>74</sup> (Fig. 2C). This dimeric structure could be independently confirmed by paramagnetic spin relaxation enhancement of amide resonances, which showed peak broadening that was consistent with inter-subunit interactions involving  $\beta$ 1 and  $\alpha$ A (Fig. S2).

The integral role for N-terminal anti-MinCD domain residues at the dimeric interface was unexpected, since the C-terminal fragment containing residues 31-88 of Ec-

MinE (Ec-TSD) forms a dimer that does not include any of these residues (12). While the Ec-TSD structure contains the  $\alpha$ B helix and  $\beta$ -strands  $\beta$ 2 and  $\beta$ 3, with the same inter-strand hydrogen bonding and side-chain interactions found in the full-length Ng-MinE structure, the dimeric interface is formed by inter-subunit hydrogen bonds between two antiparallel  $\beta$ 3 strands (Fig. 2D, 2E). The  $\alpha$ B helix also participates in extensive intersubunit interactions that are similar to those in our full-length Ng-MinE structure, with residues Ala<sup>46</sup> and Val<sup>50</sup> forming a patch at the dimeric interface analogous to that previously identified to be important for topological specificity function (Asp<sup>45</sup>/Val<sup>49</sup> in Ec-MinE) (14).

During the preparation of this manuscript, coordinates for the 2.8 Å resolution x-ray crystal structure of MinE from *Helicobacter pylori* (Hp) were released (19), showing the same fold for the main body of the Ng-MinE structure with a C $\alpha$  rmsd of 1.7 Å for regular secondary structure elements (Fig. S3, S4). Like the Ng-MinE structure, a portion of the anti-MinCD domain in the Hp-MinE structure forms a  $\beta$ -strand at the dimeric interface. In the case of the crystal structure the first 12-15 residues were not visible, preventing the observation of an inter-molecular interaction involving the N-terminal  $\alpha$ -helix. In addition, the  $\beta$ 1 interface appears to be less extensive in the crystal structure compared to that in the solution NMR structure. Specifically, the inter-molecular hydrogen-bonding network identified in the crystal structure for  $\beta$ 1 is shorter than that inferred for Ng-MinE from NOE and solvent-exchange data (Fig. 1F, S5). These structural differences may be a consequence of the shorter loops that are characteristic of proteins from extremophiles like *H. pylori*, although the potential influence of crystal packing interactions on MinE structure cannot be ruled out as a contributing factor.

### ***Identification of residues important for stimulation of MinD activity***

One of the unexpected aspects of the full-length Ng-MinE structure was the localization of residues previously identified to be important for anti-MinCD function (residues 20 to 30) at the dimeric interface (Fig. 3A). Even though they are not at all solvent accessible, mutations made at Leu<sup>22</sup> and Ile<sup>25</sup> have been shown to abrogate the ability of MinE to interact with MinD and disrupt the MinCD complex (10). As has been suggested from the Hp-MinE structure (19), a reasonable explanation for this is that these residues do not directly interact with MinD, but instead are critical for maintaining a dimeric folded state. Our NMR and CD studies on L22D Ng-MinE (17) showing significant loss of structure would be consistent with this hypothesis. Therefore, if these residues do not directly participate in MinD interactions then anti-MinCD activity must reside in the more solvent-accessible regions of the anti-MinCD domain.

To identify true MinD-binding residues in Ng-MinE, we tested the ability of a series of mutants to stimulate Ng-MinD ATPase activity in the presence of phospholipid vesicles. As shown in Figure 3A, for most mutants in the N-terminal region of Ng-MinE, no differences in stimulation of MinD ATP hydrolysis rates from WT-levels were detected. In addition, the mutant used for structure determination (E46A) also stimulated MinD activity to levels that were indistinguishable from that of WT Ng-MinE. However, two mutants previously identified to be deficient in anti-MinCD activity, namely A18D and the structurally perturbed L22D (20), showed a complete loss of MinD ATPase stimulation. R21A and K19A also showed lower activity, suggesting that the MinD interaction mainly involves the flexible loop and part of the central  $\beta$ -strand.



To determine whether any part of MinE outside of this region is also involved in MinD interactions, a peptide comprised of residues 1-22 Ng-MinE (Ng-MinE<sub>1-22</sub>) was tested for Ng-MinD ATPase activity stimulation over a range of peptide concentrations. Assuming that the rate of ATP hydrolysis is directly proportional to the amount of MinE bound, then the change in activity as a function of MinE concentration can be fit to the Hill equation. In this analysis the concentration of Ng-MinE required to reach half-maximal stimulation ( $K_{0.5}$ ) can be considered to be a measure of the relative affinity of the interaction between Ng-MinE and Ng-MinD (21). As shown in Figure 3B, both the full-length and N-terminal Ng-MinE<sub>1-22</sub> samples were capable of stimulating Ng-MinD ATPase activity to the same maximal level; however, the  $K_{0.5}$  values were significantly different between the two samples. As summarized in Table 1,  $K_{0.5}$  for full-length Ng-MinE was 0.11  $\mu$ M, while approximately five times more MinE<sub>1-22</sub> peptide was required to achieve the same level of activation. Also, the R21A mutant of this peptide, as well as a truncated version (Ng-MinE<sub>1-17</sub>), did not show any stimulation of ATPase activity, even at concentrations of 20  $\mu$ M (Fig. S6). Taken together, these results show that the residues required for maximal stimulation of MinD activity are present in residues 18-22, but that residues beyond this N-terminal region also contribute to interactions with MinD.

#### ***Investigation of the role of $\beta$ 1-residues in stimulation of MinD ATPase activity***

The ability to use peptides to test stimulation of MinD ATPase activity allowed us to address the specific role of Leu<sup>22</sup> as well as additional regions of the anti-MinCD domain in the MinD interaction. While the L22D mutant of the full-length protein was not active, this may have been due to the significant structural perturbation that results from the introduction of a negative charge in the hydrophobic core (17). However, if

Leu<sup>22</sup> plays a direct role in MinD interactions, then an L22D version of MinE<sub>1-22</sub> would also be expected to show reduced activity relative to the WT peptide, because the activity of the peptide does not require the globular core. This is in fact what was observed since MinE<sub>1-22</sub> L22D failed to stimulate MinD ATPase activity over a wide range of concentrations. To evaluate whether this effect was specific for the aspartic acid mutant, we also performed this analysis with the more conservative L22A mutant of MinE<sub>1-22</sub>. In this case although maximal MinD activity could be attained at very high concentrations of the peptide, K<sub>0.5</sub> was almost 10-fold larger than that of the WT-peptide (Table 1), providing strong evidence that Leu<sup>22</sup> participates directly in MinD interactions.

The identification of a direct role for MinD interactions involving Leu<sup>22</sup>, a residue that is in a solvent-inaccessible position of the inter-subunit interface of the Ng-MinE dimer raised the possibility that other residues in this region of the structure may also play a similar role. For this reason, a longer N-terminal peptide, MinE<sub>1-27</sub>, was tested in the same ATPase stimulation assay since it contains additional residues from that functional anti-MinCD domain that are buried in the structure. As shown in Figure 3C, this peptide was more active than Ng-MinE<sub>1-22</sub>, with a profile that was almost the same as that of the full-length protein, including a K<sub>0.5</sub> of 0.08  $\mu$ M (Table 1). To determine whether this apparent increase in affinity provided by residues 23 to 27 was specific, we repeated the experiment using a mutant that had previously been identified to be defective for anti-MinCD activity, namely I25R (10). While the I25R mutant of this peptide was capable of fully stimulating MinD activity, approximately 30-fold more peptide was required to reach half-maximal levels relative to the WT peptide (Fig. 3C, Table 1). In contrast, when I24R Ng-MinE<sub>1-27</sub> was tested in the same assay, rate profiles

were highly similar to those from the WT peptide. A smaller effect was observed for the more conservative I25A mutant of Ng-MinE<sub>1-27</sub>, although its apparent affinity was still weaker than that of the WT peptide. Overall this data provides strong evidence that Ile<sup>25</sup> is one of the residues directly involved in the interaction between full-length MinE and MinD.

### ***Evidence for conformational dynamics in MinE***

When the residues identified to be important for stimulation of Ng-MinD activity are mapped onto the Ng-MinE structure, it is apparent that many are in regions that cannot easily be accessed by a macromolecular binding partner. For example, while the side chains of Arg<sup>21</sup> and Ile<sup>25</sup> are on the same side of  $\beta$ 1, approach to these residues would be hindered by the presence of the N-terminal helix and adjacent loop (Fig. 4A). However, if MinE exists in a dynamic exchange with a more open conformation then this may provide a mechanism for MinD to bind. To examine the internal dynamics of MinE <sup>15</sup>N spin relaxation experiments were acquired. These demonstrated that the loop connecting  $\alpha$ A and  $\beta$ 1 does undergo significant backbone dynamics on the nanosecond to picosecond timescale (Fig. S7).

A series of backbone amide relaxation dispersion measurements designed to probe the presence of motion on the microsecond to millisecond timescale also revealed motions extending to other regions of the protein. Contributions to transverse relaxation from exchange processes manifest as increased line broadening that can be compensated by a Carr-Purcell-Meiboom-Gill (CPMG) spin echo pulse train sequence (reviewed in 22). Variations in the apparent transverse relaxation rate ( $R_{2,\text{eff}}$ ) as a function of CPMG pulse frequency ( $\nu_{\text{CPMG}}$ ) are indicative of conformational exchange. Our results (Fig. 4B,

C) show microsecond to millisecond timescale exchange in residues from the N-terminal helix that interact with the  $\beta$ -sheet, and in the corresponding residues within this sheet proximal to this interaction. The localization of these residues suggests a motion that could involve dissociation of the N-terminal  $\alpha$ -helix from the central  $\beta$ -sheet, a change that would significantly enhance access to Ile<sup>25</sup> and Arg<sup>21</sup> for MinD interactions. This model would also be consistent with the small surface area associated with this interaction that predicts a relatively weak association for the  $\alpha$ A helix, and with the absence of electron density for this part of the Hp-MinE crystal structure (19).

In addition to the  $\alpha$ A helix and adjacent loops, a number of residues in  $\beta$ 1 (Asp<sup>20</sup>, Leu<sup>22</sup>, Ile<sup>24</sup>) also showed evidence for dynamics on this timescale. This exchange may reflect the change in local chemical environment that would occur upon dissociation of the N-terminal helix. However, it is also possible that structural changes in these regions accompany this dissociation. Most significantly, conformational flexibility in  $\beta$ 1 could provide a mechanism for MinD to access residues such as Leu<sup>22</sup>, whose side chain is completely concealed in the hydrophobic core of the dimeric interface. Some insight into the nature of this conformational change is provided by the Hp-MinE structure (19), which shows the ends of  $\beta$ 1 diverging away from the interface (Fig. S3). Although the side chain corresponding to Leu<sup>22</sup> is still completely buried in the Hp-MinE structure, this more open state may represent an intermediate on the path toward larger structural perturbations that might be induced by MinD binding.

## Discussion

A longstanding model of the MinE-MinD interaction involving a solvent-exposed, helix-forming anti-MinCD domain (10) has been challenged by the detection of  $\beta$ -

structure in the anti-MinCD domain (17), the partial structure of Hp-MinE (19), and now by our solution NMR structure of full-length Ng-MinE. In particular, the structures show that residues previously identified to be important for anti-MinCD function are buried in the  $\beta$ 1 dimeric interface. Given the central role for this region in dimerization, it is likely that mutation of non-solvent-accessible residues in this region that were previously shown to abrogate anti-MinCD function (e.g. L22D, I25R) would significantly perturb this dimeric structure. However, the in vitro MinD ATPase activities obtained with anti-MinCD domain peptides suggest that the loss of binding affinity for MinD exhibited by these mutants is not a consequence of this structural change, but instead is primarily due to the elimination of large hydrophobic side chains that directly participate in the interaction. Therefore, in order for MinD to bind these residues in the full-length protein, some type of conformational change must occur to increase their accessibility. The conformational exchange we detected in the anti-MinCD domain does provide a mechanism for increased access to some of these MinD-binding residues. However, it is still not clear how MinD might simultaneously bind all of these residues in the dimer structure.

One scenario that could improve solvent-accessibility for MinD-binding residues that has yet to be explored is one where the MinE dimer dissociates into a monomer prior to its association with MinD. Dissociation of the dimer would give rise to a significant increase in solvent accessibility for the anti-MinCD domain that could make the monomer the higher-affinity ligand for MinD. In fact, the demonstration that the MinE<sub>1-27</sub> fragment reconstitutes in vitro MinD activation with properties that are virtually indistinguishable from that of the full-length protein is consistent with this possibility

(Fig. 2B). Previous yeast two-hybrid and gel filtration data with Ec-MinE<sub>1-31</sub> showed that this fragment does not self-associate (13), suggesting that dimerization is not necessary to stimulate MinD activity.

The dissociation constant of 0.6  $\mu$ M that was previously determined for Ec-MinE dimerization (14), does predict a significant population of monomeric MinE at concentrations that give rise to maximal MinD activation under our in vitro assay conditions ( $> 0.2 \mu$ M). However, this may not be the case for Ng-MinE, since sedimentation velocity experiments did not show evidence for a monomeric species (Fig. S8) even when sample concentrations at the limit of detection were used (3  $\mu$ M). Nonetheless, this does not rule out the presence of low concentrations of the monomer that could be sufficient for maximal stimulation of ATP hydrolysis by MinD. Moreover, the actual association properties of MinE in vivo, and under in vitro assay conditions are likely to be multifaceted. In particular, the higher-order structures formed by MinD give rise to elevated local concentrations of MinE that would be expected to favor its self-association. This effect should also be in operation in vitro, since dynamic mesostructures have been demonstrated for MinD on the surface of planar lipid bilayers, with a non-uniform co-localization of MinE (31, 32). In our assay we obtained Hill coefficients that are greater than two (Table 1), suggesting that a polymeric structure functionally linking multiple MinE-binding sites was also reconstituted under these conditions. However, in the absence of structural details for the MinD polymer it is not possible to predict whether a MinE dimer or monomer would interact more favorably. Due to these considerations, in addition to other non-specific effects that could also affect the association properties of MinE (e.g. volume exclusion/molecular crowding, lipid-

protein interactions etc), further investigation will be required to determine which oligomerization state of MinE is involved in MinD binding and E-ring formation.

Although the role of the dimeric state for MinE in the interaction with MinD is still not clear, there is one significant advantage that should be provided by the concealment of MinD-binding residues. Specifically, promiscuous interactions between MinE and other prospective binding partners should be greatly reduced by sequestering the anti-MinCD domain away from the solvent. Of particular relevance are the non-specific interactions that could be expected to occur between hydrophobic portions of the anti-MinCD domain and the membrane. It has been shown that, in contrast with full-length MinE, the isolated anti-MinCD domain (Ec-MinE<sub>1-31</sub>) localizes to the membrane *in vivo*, even in the absence of MinD (10). Similarly, mutations made to full-length Ec-MinE that should disrupt the structure at the  $\beta$ 1 interface, namely L22R, L22S and I25R, also gave rise to this same pattern of MinD-independent membrane localization. These results show that free exposure of the full anti-MinCD domain to solvent gives rise to membrane-localized MinE, and that there is no topological specificity to this localization. This would have important functional consequences, since strong interactions with the membrane could inhibit dynamic Min protein localization by preventing the free diffusion of unbound MinE through the cytoplasm that computational models suggest is a fundamental requirement for oscillation (reviewed in 29). In addition, the MinD/Par superfamily of proteins has been suggested to have a conserved mechanism for stimulation of ATPase activity (30), raising the possibility that a freely exposed anti-MinCD domain could interact with other members of this family. Whatever the potential binding partner, localization of key MinD-binding residues to the MinE dimeric interface

minimizes the potential for non-specific interactions. Sequestration of these residues away from the solvent therefore provides a mechanism to allow unhindered diffusion of MinE through the cytoplasm in regions where concentrations of membrane-bound MinD are low, allowing normal Min protein oscillation to occur.

## **Materials and Methods**

### ***Protein Expression, Purification and Mutagenesis***

Plasmids used for expression of WT, E46A, L22D, and A18D Ng-MinE and WT Ng-MinD were as described previously (17, 20). All other mutants of the full-length Ng-MinE were generated by site directed mutagenesis of the WT plasmid, using the QuikChange Site-Directed mutagenesis protocol (Stratagene). All Min protein constructs expressed Ng-Min proteins appended at the C-terminal to a sequence of eight additional residues (LEHHHHHH). Expression and purification was done as previously described (17, 20). Sedimentation velocity experiments confirmed a dimeric state for these samples (Fig. S8).

### ***In vitro MinD ATPase Assay***

Stimulation of Ng-MinD ATP hydrolysis by Ng-MinE was monitored using the malachite green method (33). Reactions contained 2.7  $\mu$ M Ng-MinD in 65 mM Tris HCl pH 8.2, 50 mM KCl, 80 mM NaCl, 1 mM ATP, 5 mM MgCl<sub>2</sub> with 500  $\mu$ g/mL 1,2-dioleoyl-sn-glycero-3-[phosphor-rac-(1-glycerol)] (DOPG) phospholipids (Avanti Polar Lipids). Concentrations of purified Ng-MinE and Ng-MinD were determined using a bicinchoninic acid (BCA) assay (Pierce Biotech). Concentrations of WT and mutant Ng-MinE peptide stock solutions (Genescript USA Inc., Piscataway, NJ) were determined



amino acid analysis (Advanced Protein Technology Centre, Hospital for Sick Children, Toronto). For the full-length Ng-MinE samples, average ATP hydrolysis rates stimulated by 0.06  $\mu\text{M}$  of the WT or indicated mutant were measured using at least two different protein preparations.

The specific Ng-MinD activity plotted as a function of increasing concentration for full-length, or N-terminal fragments of Ng-MinE generally showed a sigmoidal appearance. Assuming that the rate of Ng-MinD-stimulated ATP hydrolysis is directly proportional to the amount of MinE binding, then the ratio of the measured rate ( $v_o$ ) versus the maximal rate ( $V_{\text{max}}$ ) of MinD-stimulated ATP hydrolysis can be considered to approximate the fraction of available MinE-binding sites that are occupied ( $\theta$ ). Changes in the fraction of occupied sites for cooperative binding systems can generally be described by the Hill equation:

$$\theta = \frac{[\text{L}]_o^h}{K_{0.5}^h + [\text{L}]_o^h}$$

where  $K_{0.5}$  is the concentration of ligand (L) required to reach half-maximal saturation and  $h$  is an interaction coefficient that can reflect the level of MinE-binding cooperativity.

In our system  $\theta = \frac{v_o}{V_{\text{max}}}$  and  $[\text{L}]_o$  is the concentration of Ng-MinE used. Non-linear least squares fitting of MinE-stimulated MinD ATP hydrolysis rates allowed determination of  $V_{\text{max}}$ ,  $K_{0.5}$  and  $h$ .

### ***NMR Spectroscopy***

NMR spectra were recorded at 298 K on either a 500 or an 800 MHz Varian Unity Inova spectrometer equipped with a cryoprobe.  $^1\text{H}$ ,  $^{15}\text{N}$  and  $^{13}\text{C}$  resonance assignments were obtained for E46A Ng-MinE as described elsewhere (18). NMR

samples were typically 0.7-1.0 mM of uniformly labeled  $^{15}\text{N}$ - or  $^{13}\text{C}$ ,  $^{15}\text{N}$ -labeled E46A Ng-MinE in a buffer containing 22.5 mM Tris-HCl at pH 7.2, 45 mM NaCl, 0.1 mM EDTA, 0.2 mM benzamidine, 0.02%  $\text{NaN}_3$  and 1 mM 2,2-dimethyl-2-silapentane-5-sulphonic acid (DSS). A hetero-dimeric protein sample was also prepared by mixing equimolar amounts of  $^{15}\text{N}$ - and  $^{13}\text{C}$ -,  $^{15}\text{N}$ -labeled E46A Ng-MinE in 6 M guanidinium hydrochloride. This sample was refolded on a Ni-NTA column by a stepwise buffer exchange into denaturant-free buffer and repurified by size-exclusion chromatography.

Measurement of one-bond  $^1\text{H}$ - $^{15}\text{N}$  residual dipolar couplings (RDCs) of backbone amides was done using a stretched 3% (w/v) polyacrylamide gel (34) with in-phase/anti-phase single-quantum coherence ( $^{15}\text{N}$ -IPAP-HSQC) spectra (35). Spectra were processed and analyzed using NMRPipe, (36), NMRView (37), and SPARKY (T. D. Goddard and D. G. Kneller, SPARKY 3, University of California, San Francisco).

### ***Structure Calculation***

NOE distance restraints were inferred from 3D  $^{15}\text{N}$ -edited NOESY-HSQC ( $\tau_{\text{mix}} = 100$  ms) (38-40), aliphatic  $^{13}\text{C}$ -edited NOESY HSQC ( $\tau_{\text{mix}} = 80$  ms) (41) and 3D  $^{13}\text{C}$ -edited methyl-methyl NOESY ( $\tau_{\text{mix}} = 75$  ms) (42) spectra, and used in the molecular simulation program XPLOR-NIH (43) to generate an initial model for E46A Ng-MinE. This model was then used as the starting structure for the torsion angle dynamics program CYANA 2.1 (44) and the automatic NOE assignment invoked to calculate 200 conformers. Based on hydrogen exchange data and the presence of characteristic secondary structure NOEs (17), 26 hydrogen bonds/subunit were also added to the restraint set. A total of 1849 unique and non-redundant NOE distance constraints/subunit were generated from the NOESY spectra. In addition, 68 inter-molecular upper-bound

restraints per subunit derived from 3D F1- $^{13}\text{C}$ ,  $^{15}\text{N}$ -filtered/F3- $^{13}\text{C}$  edited NOESY spectrum ( $\tau_{\text{mix}} = 80$  ms) (45) were added as input restraints.

XPLOR-NIH was subsequently used to subject the structure with the lowest target-function value from CYANA 2.1 to refinement against measured  $^1\text{H}$ - $^{15}\text{N}$  RDCs. Phi/Psi dihedral angles which were derived from the program TALOS (46) were also included in the set of constraints. The ten lowest energy structures from a calculation of 200 structures was used to represent the NMR ensemble (statistics in Table S1).

### ***$^{15}\text{N}$ Relaxation Dispersion Experiments***

In order to evaluate chemical exchange, an improved version (47) of the  $^{15}\text{N}$  CPMG (48, 49) pulse sequence was employed at 30 °C and two magnetic fields (500 and 800 MHz), using a CPMG relaxation delay time of 30 ms. Effective relaxation rates  $R_2^{\text{eff}}$  were determined from peak intensities as previously described (50). Uncertainty in effective relaxation rates were estimated from duplicates. Assuming a two-state exchange model, the relaxation rates were fitted on a per-residue basis using CATIA (available from <http://pound.med.utoronto.ca/software.html>).

### **Acknowledgements**

This work was supported by a CIHR operating grant to NKG and JRD (MOP-160206), and an Early Researcher Award to NKG. HG was supported the Sweden-America Foundation and Knut and Alice Wallenberg Foundation, and CTH by an Ontario Graduate Scholarship. NC and AAB are both recipients of NSERC Undergraduate Research Scholarships. For expert technical assistance we acknowledge Dr. Tara Sprules at the Quebec/Eastern Ontario High Field NMR facility in Montreal, Québec, and Kim

Munro at the Protein Function Discovery facility. We are grateful to Anthony Mittermaier for helpful discussions, and Lewis Kay for critical reading of this manuscript.

## References

1. Lutkenhaus, J (2008) Min oscillation in bacteria. *Adv Exp Med Biol* 641: 49-61.
2. Hu, Z, Lutkenhaus, J (1999) Topological regulation of cell division in *Escherichia coli* involves rapid pole to pole oscillation of the division inhibitor MinC under the control of MinD and MinE. *Mol Microbiol* 34: 82-90.
3. Raskin, DM, de Boer, PA (1999) MinDE-dependent pole-to-pole oscillation of division inhibitor MinC in *Escherichia coli*. *J Bacteriol* 181: 6419-6424.
4. Raskin, DM, de Boer, PA (1999) Rapid pole-to-pole oscillation of a protein required for directing division to the middle of *Escherichia coli*. *Proc Natl Acad Sci USA* 96: 4971-4976.
5. Shih, YL, Le, T, Rothfield, L (2003) Division site selection in *Escherichia coli* involves dynamic redistribution of Min proteins within coiled structures that extend between the two cell poles. *Proc Natl Acad Sci USA* 100: 7865-7870.
6. Szeto, J, et al. (2005) A conserved polar region in the cell division site determinant MinD is required for responding to MinE-induced oscillation but not for localization within coiled arrays. *Res Microbiol* 156: 17-29.
7. Fu, X, Shih, YL, Zhang, Y, Rothfield, LI (2001) The MinE ring required for proper placement of the division site is a mobile structure that changes its cellular location during the *Escherichia coli* division cycle. *Proc Natl Acad Sci USA* 98: 980-985.
8. Hale, CA, Meinhardt, H, de Boer, PA (2001) Dynamic localization cycle of the cell division regulator MinE in *Escherichia coli*. *EMBO J* 20: 1563-1572.

9. Hu, Z, Lutkenhaus, J (2001) Topological regulation of cell division in *E. coli*. Spatiotemporal oscillation of MinD requires stimulation of its ATPase by MinE and phospholipid. *Mol Cell* 7: 1337-1343.
10. Ma, LY, King, G, Rothfield, L (2003) Mapping the MinE site involved in interaction with the MinD division site selection protein of *Escherichia coli*. *J Bacteriol* 185: 4948-4955.
11. King, GF, et al. (1999) The dimerization and topological specificity functions of MinE reside in a structurally autonomous C-terminal domain. *Mol Micro* 31: 1161-1169.
12. King, GF, et al. (2000) Structural basis topological specificity function of MinE. *Nat Struct Biol* 7: 1013-1017.
13. Pichoff, S, Vollrath, B, Touriol, C, Bouché, JP (1995) Deletion analysis of gene *MinE* which encodes the topological specificity factor of cell division in *Escherichia coli*. *Mol Microbiol* 18: 321-329.
14. Zhang, Y, et al. (1998) The relationship between hetero-oligomer formation and function of the topological specificity domain of the *Escherichia coli* MinE protein. *Mol Microbiol* 30: 265-273.
15. Zhao, CR, De Boer, PA, Rothfield, LI (1995) Proper placement of the *Escherichia coli* division site requires two functions that are associated with different domains of the MinE protein. *Proc Natl Acad Sci USA* 92: 4313-4317.
16. King, GF, et al. (1999) The dimerization and topological specificity functions of MinE reside in a structurally autonomous C-terminal domain. *Mol Microbiol* 31: 1161-1169.

17. Ramos, D, et al. (2006) Conformation of the cell division regulator MinE: evidence for interactions between the topological specificity and anti-MinCD domains. *Biochemistry* 45: 4593-4601.
18. Ducat, T, Goto, NK (2010) <sup>1</sup>H, <sup>13</sup>C, <sup>15</sup>N chemical shift assignments for the *Neisseria gonorrhoeae* MinE regulator of cell division septum placement. *Biomol NMR Assign* Submitted.
19. Kang, GB, et al. (2010) Crystal structure of *Helicobacter pylori* MinE, a cell division topological specificity factor. *Mol Microbiol* Epub.
20. Eng, NF, et al. (2006) The C-terminus of MinE from *Neisseria gonorrhoeae* acts as a topological specificity factor by modulating MinD activity in bacterial cell division. *Res Microbiol* 157: 333-344.
21. Weiss, JN (1997) The Hill equation revisited: uses and misuses. *FASEB J* 11: 835-841.
22. Mittermaier, A, Kay, LE (2006) New tools provide new insights in NMR studies of protein dynamics. *Science* 312: 224-228.
23. Burrows, SD, et al. (1994) Determination of the monomer-dimer equilibrium of interleukin-8 reveals it is a monomer at physiological concentrations. *Biochemistry* 33: 12741-12745.
24. Baldwin, ET, et al. (1991) Crystal structure of interleukin 8: Symbiosis of NMR and crystallography. *Proc Natl Acad Sci USA* 88: 502-506.
25. Clore, GM, et al. (1990) Three-dimensional structure of interleukin 8 in solution. *Biochemistry* 29: 1689-1696.

26. Rajarathnam, K, Clark-Lewis, I, Sykes, BD (1995)  $^1\text{H}$  NMR solution structure of an active monomeric interleukin-8. *Biochemistry* 34: 12983–12990.
27. Rajarathnam, K, et al. (2006) Probing receptor binding activity of interleukin-8 dimer using a disulfide trap. *Biochemistry* 45: 7882-7888.
28. Ravindran, A, Joseph, PR, Rajarathnam, K (2009) Structural basis for differential binding of the interleukin-8 monomer and dimer to the CXCR1 N-domain: role of coupled interactions and dynamics. *Biochemistry* 48: 8795-8805.
29. Kruse, K, Howard, M, Margolin, W (2007) An experimentalist's guide to computational modelling of the Min system. *Mol Microbiol* 63: 1279-1284.
30. Leonard, TA, Butler, PJ, Löwe, J (2005) Bacterial chromosome segregation: structure and DNA binding of the Soj dimer--a conserved biological switch. *EMBO J* 24: 270-282.
31. Ivanov, V, Mizuuchi, K (2010) Multiple modes of interconverting dynamic pattern of formation by bacterial cell division proteins. *Proc Natl Acad Sci USA* 107: 8071-8078.
32. Loose, M, et al. (2008) Spatial regulators for bacterial cell division self-organize into surface waves in vitro. *Science* 320: 789-792.
33. Harder, KW, et al. (1994) Characterization and kinetic analysis of the intracellular domain of human protein tyrosine phosphatase beta (HPTP-beta) using synthetic phosphopeptides. *Biochem J* 298: 395-401.
34. Chou, JJ, et al. (2001) A simple apparatus for generating stretched polyacrylamide gels, yielding uniform alignment of proteins and detergent micelles. *J Biomol NMR* 21: 377-382.



35. Ottiger, M, Delaglio, F, Bax, A (1998) Measurement of J and dipolar couplings from simplified two-dimensional NMR spectra. *J Magn Reson* 131: 373-378.
36. Delaglio, F, et al. (1995) NMRPipe: a multidimensional spectral processing system based on UNIX pipes. *J Biomol NMR* 6: 277-293.
37. Johnson, BA, Blevins, RA (1994) NMRView: a computer program for the visualization and analysis of NMR data. *J Biomol NMR* 4: 603-614.
38. Marion, D, et al. (1989) Three-dimensional heteronuclear NMR of <sup>15</sup>N-labeled proteins *J Am Chem Soc* 111: 1515-1517.
39. Talluri, S, Wagner, G (1996) An optimized 3D NOESY-HSQC. *J Magn Reson B* 112: 200-205.
40. Zhang, O, Kay, LE, Olivier, JP, Forman-Kay, JD (1994) Backbone <sup>1</sup>H and <sup>15</sup>N resonance assignments of the N-terminal SH3 domain of drk in folded and unfolded states using enhanced-sensitivity pulsed field gradient NMR techniques. *J Biomol NMR* 4: 845-858.
41. Muhandiram, DR, et al. (1993) A gradient <sup>13</sup>C NOESY-HSQC experiment for recording NOESY spectra of <sup>13</sup>C-labeled proteins dissolved in H<sub>2</sub>O *J Magn Reson B* 102: 317-321.
42. Zwahlen, C, et al. (1998) An NMR experiment for measuring methyl-methyl NOEs in <sup>13</sup>C-labeled proteins with high resolution. *J Am Chem Soc* 120: 7617-7625.
43. Schwieters, CD, Kuszewski, JJ, Tjandra, N, Clore, GM (2003) The Xplor-NIH NMR molecular structure determination package. *J Magn Reson* 160: 65-73.

44. Güntert, P (2004) Automated NMR structure calculation with CYANA. *Methods Mol Biol* 278: 353-378.
45. Zwahlen, C, et al. (1997) Methods for measurement of intermolecular NOEs by multinuclear NMR spectroscopy: application to a bacteriophage  $\lambda$  N-peptide/*boxB* RNA complex. *J Am Chem Soc* 119: 6711–6721.
46. Cornilescu, G, Delaglio, F, Bax, A (1999) Protein backbone angle restraints from searching a database for chemical shift and sequence homology. *J Biomol NMR* 13: 289-302.
47. Hansen, DF, Vallurupalli, P, Kay, LE (2008) An improved  $^{15}\text{N}$  relaxation dispersion experiment for the measurement of millisecond time-scale dynamics in proteins. *J Phys Chem B* 112: 5898-5904.
48. Carr, HY, Purcell, EM (1954) Effects of diffusion on free precession in nuclear magnetic resonance experiments. *Phys Rev* 94: 630-638.
49. Meiboom, S, Gill, D (1958) Modified spin-echo method for measuring nuclear relaxation times. *Rev Sci Instrum* 29: 688-691.
50. Tollinger, M, et al. (2001) Slow dynamics in folded and unfolded states of an SH3 domain. *J Am Chem Soc* 123: 11341-11352.

## Figure Legends

### *Figure 1*

A) Model of Min protein oscillation in rod-shaped bacteria. MinD forms a coiled array (red) that extends from the cell pole and is capped by a MinE-rich region known as the E-ring (blue). Disassembly of the array towards the cell pole (in the direction of the blue arrow) is accompanied by assembly of a new MinD coil at the opposing pole (red arrow).

B) Schematic diagram of the Min cycle. (1) MinD (purple) bound to ADP (light blue) undergoes nucleotide exchange with ATP (yellow), to give rise to a membrane-bound state that can bind MinC (red), the inhibitor of cell division septum formation. (2) MinE (blue) binding to MinD displaces MinC and (3) stimulates ATP hydrolysis by MinD to release inorganic phosphate (green). MinE is released from the complex while ADP-bound MinD also dissociates from the membrane, allowing the cycle to begin again.

C) Functional domain structure of MinE. Residues 1-30 comprise the anti-MinCD (ACD) domain while the remaining C-terminal residues contain the topological specificity domain (TSD).

### *Figure 2*

A) Ribbon diagram representation of the Ng-MinE structure determined by solution NMR, with the two views related by a 180° rotation. Each subunit is shown in either blue or purple, and anti-MinCD residues 1-30 that encompass  $\alpha$ A and  $\beta$ 1 are darker shades of these colors. Side chains for residues corresponding to those previously identified to be important for topological specificity function (Glu<sup>46</sup>, which is mutated to Ala in this structure, and Val<sup>50</sup>) are shown as balls.

B) Detailed view of the dimeric  $\alpha$ B interface, highlighting residues participating in inter-helical interactions.

C) Electrostatic surface

representation for residues 20-84, in the same orientation as that shown on the right hand side of panel A. The N-terminal  $\alpha$ -helices (ribbons) pack against small hydrophobic patches that are flanked by negatively charged residues (red) that could attract the positively charged N-terminus. D) Schematic diagram highlighting the integral role for anti-MinCD residues 19 - 31 in the dimeric Ng-MinE  $\beta$ -sheet. The orientation and color scheme is the same as in the right hand side of panel A. Amino acids forming inter-strand backbone hydrogen bonds are linked by a solid line, with orange lines indicating hydrogen bonds that were also observed for homologous residues in the Ec-TSD structure (12). Residues homologous to those involved in inter-subunit hydrogen bonds in the Ec-TSD structure are shown in orange. E) Structure of Ec-TSD (PDB ID 1EV0) with secondary structure elements homologous to those in the Ng-MinE structure indicated with labels. The pairwise C $\alpha$  rmsd for a single subunit of Ec-TSD and Ng-MinE is 2.9 Å (regular secondary structure elements only). F) Amide protons that could be observed in  $^1\text{H}$ - $^{15}\text{N}$  HSQC spectra of WT Ng-MinE recorded at pH 9.5 (20) are highlighted in blue, indicating residues that are protected from base-catalyzed solvent exchange due to hydrogen-bonding. The region corresponding to the part of the Hp structure engaged in inter-molecular backbone hydrogen-bonding interactions is shown in green for comparison.

### ***Figure 3***

Specific activity of Ng-MinD stimulated by Ng-MinE determined in vitro. A) Comparison of activity stimulated by either WT Ng-MinE or the indicated mutant. For most mutants there was a ~10-fold increase in MinD ATPase activity compared to basal levels measured in the absence of MinE, similar to previous observations (9, 20). B)

Concentration-dependence of in vitro Ng-MinD specific activity for full-length Ng-MinE (open squares), Ng-MinE<sub>1-22</sub> (grey triangles) and MinE<sub>1-27</sub> (filled circles). C) Same as B) for Ng-MinE<sub>1-27</sub> I25R (filled circles) or I24R (open circles) mutant peptides. Lines represent best-fit curves to the Hill equation.

**Figure 4**

A) Residues important for stimulation of MinD-catalyzed hydrolysis are either partly solvent accessible (yellow side chains) or completely inaccessible (red) in the dimeric structure of full-length Ng-MinE. B) Representative relaxation dispersion curves for backbone amide groups at 800 MHz (red) and 500 MHz (black) shown for the three residues indicated. C) Backbone amides undergoing statistically significant exchange (described in the Materials and Methods) are shown as balls, where the diameter is linearly scaled according to the measured exchange rate ( $300 \text{ s}^{-1}$  -  $3100 \text{ s}^{-1}$ ). Most exchange sites cluster to a contiguous region on each end of the dimer (yellow). A structurally distinct site of exchange was also detected for  $\alpha$ C (white). No exchange was detected for amides in the  $\alpha$ B helices.

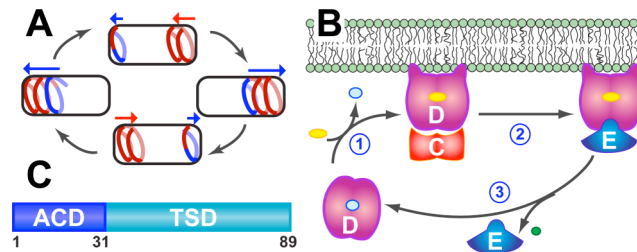


**Figure 1**

A) Model of Min protein oscillation in rod-shaped bacteria. MinD forms a coiled array (red) that extends from the cell pole and is capped by a MinE-rich region known as the E-ring (blue). Disassembly of the array towards the cell pole (in the direction of the blue arrow) is accompanied by assembly of a new MinD coil at the opposing pole (red arrow). B) Schematic diagram of the Min cycle. (1) MinD (purple) bound to ADP (light blue) undergoes nucleotide exchange with ATP (yellow), to give rise to a membrane-bound state that can bind MinC (red), the inhibitor of cell division septum formation. (2) MinE (blue) binding to MinD displaces MinC and (3) stimulates ATP hydrolysis by MinD to release inorganic phosphate (green). MinE is released from the complex while ADP-bound MinD also dissociates from the membrane, allowing the cycle to begin again. C) Functional domain structure of MinE. Residues 1-30 comprise the anti-MinCD (ACD) domain while the remaining C-terminal residues contain the topological specificity domain (TSD).

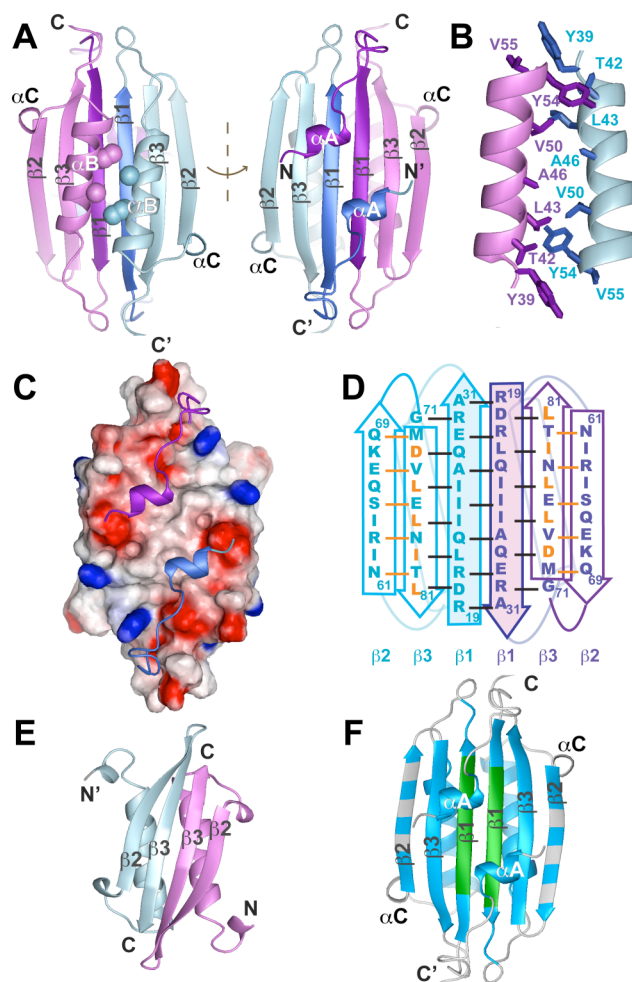


**Figure 2**

A) Ribbon diagram representation of the Ng-MinE structure determined by solution NMR, with the two views related by a  $180^\circ$  rotation. Each subunit is shown in either blue or purple, and anti-MinCD residues 1-30 that encompass  $\alpha A$  and  $\beta 1$  are darker shades of these colors. Side chains for residues corresponding to those previously identified to be important for topological specificity function (Glu<sup>46</sup>, which is mutated to Ala in this structure, and Val<sup>50</sup>) are shown as balls. B) Detailed view of the dimeric  $\alpha B$  interface, highlighting residues participating in inter-helical interactions. C) Electrostatic surface representation for residues 20-84, in the same orientation as that shown on the right hand side of panel A. The N-terminal  $\alpha$ -helices (ribbons) pack against small hydrophobic patches that are flanked by negatively charged residues (red) that could attract the positively charged N-terminus. D) Schematic diagram highlighting the integral role for anti-MinCD residues 19 - 31 in the dimeric Ng-MinE  $\beta$ -sheet. The orientation and color scheme is the same as in the right hand side of panel A. Amino acids forming inter-strand backbone hydrogen bonds are linked by a solid line, with orange lines indicating hydrogen bonds that were also observed for homologous residues in the Ec-TSD structure {King, 2000 #7}. Residues homologous to those involved in inter-subunit hydrogen bonds in the Ec-TSD structure are shown in orange. E) Structure of Ec-TSD (PDB ID 1EV0) with secondary structure elements homologous to those in the Ng-MinE structure indicated with labels. The pairwise C $\alpha$  rmsd for a single subunit of Ec-TSD and Ng-MinE is 2.9 Å (regular secondary structure elements only). F) Amide protons that could be observed in  $^1\text{H}$ - $^{15}\text{N}$  HSQC spectra of WT Ng-MinE recorded at pH 9.5 (20) are highlighted in blue, indicating residues that are protected from base-catalyzed solvent exchange due to

hydrogen-bonding. The region corresponding to the part of the Hp structure engaged in inter-molecular backbone hydrogen-bonding interactions is shown in green for comparison.

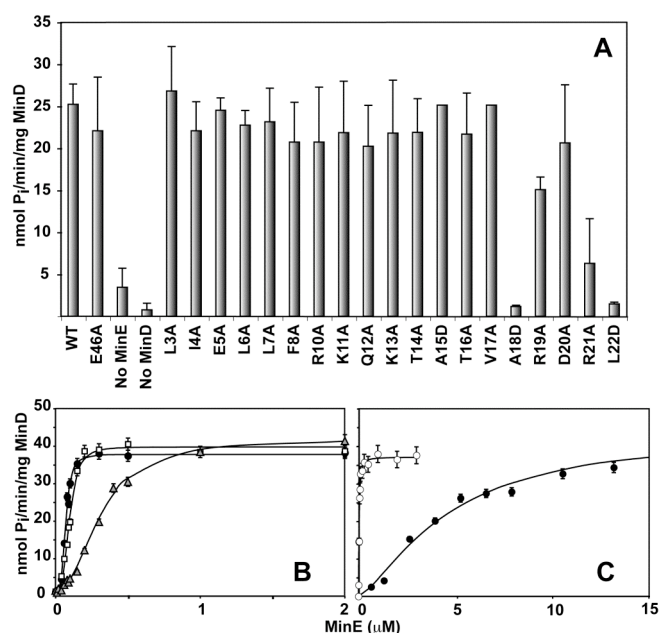


**Figure 3**

Specific activity of Ng-MinD stimulated by Ng-MinE determined in vitro. A) Comparison of activity stimulated by either WT Ng-MinE or the indicated mutant. For most mutants there was a ~10-fold increase in MinD ATPase activity compared to basal levels measured in the absence of MinE, similar to previous observations (9, 20). B) Concentration-dependence of in vitro Ng-MinD specific activity for full-length Ng-MinE (open squares), Ng-MinE<sub>1-22</sub> (grey triangles) and MinE<sub>1-27</sub> (filled circles). C) Same as B) for Ng-MinE<sub>1-27</sub> I25R (filled circles) or I24R (open circles) mutant peptides. Lines represent best-fit curves to the Hill equation.

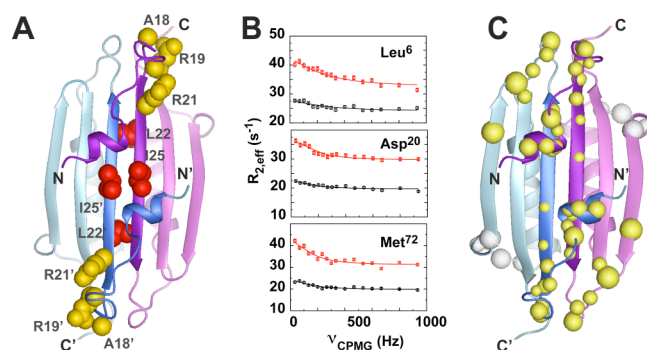


**Figure 4**

A) Residues important for stimulation of MinD-catalyzed hydrolysis are either partly solvent accessible (yellow side chains) or completely inaccessible (red) in the dimeric structure of full-length Ng-MinE. B) Representative relaxation dispersion curves for backbone amide groups at 800 MHz (red) and 500 MHz (black) shown for the three residues indicated. C) Backbone amides undergoing statistically significant exchange (described in the Materials and Methods) are shown as balls, where the diameter is linearly scaled according to the measured exchange rate (300 s<sup>-1</sup> - 3100 s<sup>-1</sup>). Most exchange sites cluster



to a contiguous region on each end of the dimer (yellow). A structurally distinct site of exchange was also detected for  $\alpha$ C (white). No exchange was detected for amides in the  $\alpha$ B helices.

## Supplemental Materials and Methods

### *Paramagnetic Relaxation Enhancement Experiments*

MinE has no native cysteine residues, and so sites for the introduction of single-cysteine mutations in E46A Ng-MinE were chosen that had high solvent accessibility, were proximal to regions of structural interest, and did not participate in structurally important interactions. Ng-MinE double mutants E46A/A31C and E46A/E83C were generated for this purpose.  $^{15}\text{N}$ -labeled samples prepared as done for other Ng-MinE proteins except that 1 mM  $\beta$ -mercaptoethanol was included in the nickel affinity purification buffers, and 1 mM dithiothreitol in the size exclusion chromatography purification buffers.  $^1\text{H}$ - $^{15}\text{N}$  HSQC spectra were acquired to confirm that only residues in close proximity to the mutated site showed chemical shift perturbations, and therefore that no structural change was caused by these mutations. Chemical shift assignments were obtained using previously assigned spectra for E46A (1).

After removal of DTT from each sample by buffer exchange in an ultracentrifugation unit, a 10% (w/v) solution of the spin-label (1-oxyl-2,2,5,5-tetramethyl-3-pyrroline-3-methyl) methanethiosulfonate (MTSL, Toronto Research Chemicals) in acetonitrile was added to a 10:1 spin label:Ng-MinE molar ratio. The final concentration of acetonitrile in the sample was typically less than 1% (v/v). After overnight incubation at room temperature, excess spin-label was removed by buffer exchange on a NAP-10 gel filtration column (GE Healthcare Life Sciences) equilibrated in 25 mM Tris pH 7.2, 50 mM NaCl, 200  $\mu\text{M}$  EDTA, 200  $\mu\text{M}$  benzamidine and 0.02%  $\text{NaN}_3$  in 10%  $\text{D}_2\text{O}$ .

$^1\text{H}$ - $^{15}\text{N}$  HSQC spectra of 350, 500 and 700  $\mu\text{M}$  paramagnetic spin-labeled mutant samples were acquired. The spin-label was subsequently reduced with a 2-4-fold molar excess of ascorbic acid and a spectrum of the reduced sample was recorded. Peak fitting was carried out

with the nlinLS module in NMRPipe (2) using a Gaussian model and the ratio of peak intensities in paramagnetic and diamagnetic spectra were determined. Measured intensity ratios were normalized using the three highest intensity ratios as has been done previously (3), to correct for decreased peak intensities in reduced spectra due to a small amount of precipitation that sometimes occurred during acquisition. Intensity ratios for the three samples were averaged and classified as strongly broadened (intensity ratio  $<0.2$ ) intermediate broadening ( $0.2-0.8$ ), or weakly broadened ( $>0.8$ ) and mapped onto the structures shown in Figure S1.

### ***Amide Exchange Experiments***

Slowly exchanging amides were monitored in  $^2\text{H}/^1\text{H}$  exchange experiments that were initiated by buffer exchange of a 0.7 mM Ng-MinE E46A sample into 25 mM Tris pH 7.2, 50 mM NaCl, 0.1 mM EDTA, 99.9% D<sub>2</sub>O using a NAP-10 column. Fourteen  $^1\text{H}$ - $^{15}\text{N}$  HSQC spectra were recorded over three days and the decay of integrated peak volumes was fit using non-linear least-squares fitting to extract proton exchange constants. Rapidly exchanging amides were monitored in the CLEANEX-PM  $^1\text{H}/^1\text{H}$  exchange experiments. A series of 10 spectra were collected with CLEANEX mixing times ranging from 5 to 90 ms and normalized peak volumes were used to extract proton exchange constants. Amide proton protection factors were calculated by dividing intrinsic exchange rate constants estimated from the program SPHERE (<http://www.fccc.edu/research/labs/roder/sphere/>) from experimentally determined proton exchange constants.

### ***Fast Motion Dynamics and Model-Free Analysis***

Standard pulse sequences (4) were used for measurements of heteronuclear steady-state  $\{^1\text{H}\}^{15}\text{N}$  NOE, longitudinal ( $^{15}\text{N}$   $R_1$ ), and transverse ( $^{15}\text{N}$   $R_2$ ) relaxation rates for  $^{15}\text{N}$ -labeled Ng-MinE (E46A) at 25 °C and a magnetic field corresponding to 500 MHz  $^1\text{H}$  Larmor frequency. The

relaxation delays used in the  $T_1$  experiments were: 10, 70, 140, 250, 360, 530, 750 and 1150 ms, and the ones in the  $T_2$  experiments were: 10, 30, 50, 70, 90, 110, 130, and 150 ms. Two sets of experiments, with inter-scan delays (d1) of 1 and 3 s, respectively, were recorded. Relaxation rates were determined by non-linear least-squares fits of data assuming a mono-exponential decay and the errors in the rates were estimated from the recorded duplicates. The  $\{^1\text{H}\}^{15}\text{N}$  NOE was measured from pairs of spectra with and without  $^1\text{H}$  saturation during a 3 s recycle delay. Relaxation data were fitted to the extended Lipari-Szabo spectral density function (5-7) employing TENSOR2 (8) using an axially symmetric anisotropic model with axial and equatorial rotational diffusion tensor components of  $D_{\parallel} \sim (1.7 \pm 0.1) \times 10^7 \text{ s}^{-1}$  and  $D_{\perp} \sim (1.2 \pm 0.1) \times 10^7 \text{ s}^{-1}$ , respectively. The relative dimensions of this tensor agree exactly with structure-based predictions using HYDRONMR with  $D_{\parallel}/D_{\perp} = 1.4$  {de la Torre, 2000 #72}.

### ***Analytical Ultracentrifugation***

Sedimentation velocity experiments were performed at the Protein Function Discovery Facility at Queen's University on a Beckman Optima XL-I instrument equipped with an An-Ti 60 rotor spun at 50,000 rpm, 20°C. Samples containing 110  $\mu\text{M}$  WT Ng-MinE in 50 mM Tris pH 8.0, 30 mM NaCl, or 3  $\mu\text{M}$  Ng-MinE in 25 mM Tris pH 8.5, 100 mM NaCl, 0.1 M EDTA were monitored with 150 scans by absorbance at 280 nm, or 450 scans by interference optics, respectively. Sedimentation profiles were generated by fitting the data to a continuous distribution  $c(S)$  Lamm equation model using the program SEDFIT {Schuck et al, 2000}.

## Supplemental Figure Legends

### *Figure S1*

Sample strips from the  $^{13}\text{C}$ -filtered/edited NOESY {Zwahlen, 1997 #42} recorded on a  $^{12}\text{C}/^{13}\text{C}$ -labeled Ng-MinE heterodimer showing intermolecular NOEs between the N-terminal  $\alpha\text{A}$  helix and the  $\beta$ -sheet. Negative intensities arise from peaks that are folded in the carbon dimension. The corresponding region of the structure is highlighted on the right. Note that the Ala27 side chain is directly under helix  $\alpha\text{A}$  in this view, on the same strand and directly above Ile25.

### *Figure S2*

Paramagnetic relaxation enhancement confirms the Ng-MinE fold contains  $\beta\text{1}$  in the dimeric interface and an N-terminal  $\alpha$ -helix interacting with the  $\beta$ -sheet. Mutations to cysteine were made either to Ala31 (top row) or Glu83 (bottom row), and samples were derivitized with the sulhydryl-reactive MTSL spin-label. The ratio of peak intensities in  $^1\text{H}$ - $^{15}\text{N}$  HSQC spectra recorded before and after reduction of the spin label provide a measure of the distance between each amide proton and the spin label (11). Residues with amide peak intensity ratios  $<0.2$  that would be within  $<15$  Å of the nitroxide spin label are colored in red,  $0.2 - 0.8$  ( $\sim 15$ - $20$  Å) in yellow, and  $>0.8$  ( $>20$  Å) in green for the Ng-MinE structure determined in this work (2 views shown on the left), or for homologous residues in the Ec-TSD structure (2 views shown on the right). Residues for which broadening could not be accurately measured due to peak overlap or missing intensities are shown in grey. Secondary structure elements homologous to those determined in the Ng-MinE structure are labeled in the Ec-TSD structure. Regions of the Ec-TSD structure that are not consistent with the spin-label induced broadening are highlighted in blue. (For clarity, only one of the two symmetric sites in the dimer is highlighted.) Specifically, for A31C, strong broadening was observed for a cluster of residues that would be at least  $\sim 20$  Å

away from the spin label in the TSD structure, but only 10 Å away in the Ng-MinE structure. For spin-labeled E83C, residues 32-35 are ~20 Å away from the side chain at position 83 in the Ec-TSD structure, but were strongly broadened. In the Ng-MinE structure these residues are 10 Å or closer to the Glu<sup>83</sup> side chain. Also, residues 68-71 showed weak to moderate broadening, but are within ~10 Å of the side chain atoms of residue 83 in the Ec-TSD structure. In the Ng-MinE structure these residues are within 15 to 20 Å of this side chain, which again is consistent with the broadening observed. Overall, these results provide independent confirmation that the topological specificity domain dimer interface involving  $\beta$ 3 is not formed in the structure of the full-length protein. All structure figures were prepared with MOLMOL (12)

### ***Figure S3***

Three views of an overlay of backbone traces for the Hp-MinE structure in red (PDB ID 3KU7) and the lowest energy member of the Ng-MinE ensemble (2KXO) in blue. The C $\alpha$  RMSD between our NMR ensemble and the 2.8 Å resolution Hp-MinE crystal structure (3KU7) was  $1.73 \pm 0.05$  Å (calculated using regular secondary structure elements Arg<sup>21</sup>-Arg<sup>30</sup>, Leu<sup>40</sup>-Tyr<sup>54</sup>, Asn<sup>61</sup>-Gln<sup>66</sup>, and Asp<sup>73</sup>-Leu<sup>81</sup> in Ng-MinE, and Arg<sup>19</sup>-Arg<sup>28</sup>, Met<sup>35</sup>-Tyr<sup>49</sup>, Asp<sup>54</sup>-Thr<sup>59</sup>, and Glu<sup>67</sup>-Leu<sup>75</sup> in Hp-MinE ). The first 18 and last 7 residues of the Ng-MinE structure were removed to facilitate visualization. Electron density that is missing for Hp-MinE residues 68-70 are indicated in the middle panel with dashed lines. The view on left has C-termini in front while the view on the right has the N-termini in front. The middle view shows the  $\beta$ 2 strand from Hp-MinE diverging significantly from that of the Ng-MinE structure, possibly due to crystal packing contacts involving  $\beta$ 3, or the absence of the N-terminal  $\alpha$ -helix that was found to interact with this part of the sheet in the Ng-MinE structure.

### ***Figure S4***

Sequence alignment from Clustal W (13) for MinE proteins from a range of pathogens, with residues showing 100% identity highlighted in orange. Dark yellow highlights the most commonly occurring residue at each position, and light yellow are homologous residues at these positions. Corresponding secondary structure elements found in the Ng-MinE structure are shown on the top, and for Hp-MinE on the bottom. Residues we identified as important for stimulation of MinD-catalyzed ATP hydrolysis are indicated with asterisks. Species abbreviations are: Ng, *Neisseria gonorrhoeae*; Ec *Escherichia coli*; Se, *Salmonella enterica*; Kp, *Klebsiella pneumoniae*; Yp, *Yersinia pestis*; Pm, *Proteus mirabilis*; Vc, *Vibrio cholerae*; Pa, *Pseudomonas aeruginosa*; Lp, *Legionella pneumophila*; Bp, *Bordetella pertussis*; Ft, *Francisella tularensis*; Ab, *Acinetobacter baumannii*; Hp, *Helicobacter pylori*.

#### **Figure S5**

Log protection factors (PF) for Ng-MinE E46A at pH 7.2, 30°C determined by  $^2\text{H}/^1\text{H}$  exchange (PF>6, purple, PF>5 dark blue, PF>4 light blue) or  $^1\text{H}/^1\text{H}$  experiments in  $\text{H}_2\text{O}$  (PF<2 orange). Residues that undergo exchange at rates that were too rapid to detect by  $^2\text{H}/^1\text{H}$  exchange and too slow to measure in  $^1\text{H}/^1\text{H}$  exchange experiments are in grey, providing indirect evidence for protection factors in the range of 2 - 4 for these regions of the structure. (Figure to be refined.)

#### **Figure S6**

Malachite green assay results for ATP hydrolysis stimulated by 3.0  $\mu\text{M}$  WT or 20  $\mu\text{M}$  mutant Ng-MinE<sub>1-22</sub>, or 20  $\mu\text{M}$  Ng-MinE<sub>1-17</sub> peptide. Absorbance at 620 nm was measured for aliquots that were removed at four different time points, centrifuged to remove the lipid vesicles, mixed with the malachite green reagent and allowed to develop for 15 minutes prior to taking the absorbance reading. Only the wild-type peptide showed an increased rate of ATP hydrolysis over basal levels.

### ***Figure S7***

Backbone amide  $^{15}\text{N}$  relaxation values measured for Ng-MinE (E46A) at 25°C.  $^{15}\text{N}$   $R_1$  and  $R_2$  relaxation rates (A and B),  $^1\text{H}$ - $^{15}\text{N}$  heteronuclear NOEs (C), and generalized order parameters,  $S^2$  (D), are shown as a function of residue number. Residues at the C-terminus and in the loop between  $\alpha\text{A}$  and  $\beta\text{1}$  showed the presence of significant dynamics on the ps to ns timescale. Order parameter and heteronuclear NOE values for residues in the N-terminal  $\alpha\text{A}$  helix are similar to those obtained for the main body of the structure, confirming the stable association of these structural elements.

### ***Figure S8***

Sedimentation velocity experiment showing a predominantly dimeric state for WT Ng-MinE at 110  $\mu\text{M}$  (red), and 3  $\mu\text{M}$  (blue). The sedimentation coefficient for the main species is 1.91 - 1.92 S, corresponding to a molecular weight of 22.0 - 22.2 kDa. The expected molecular mass for the His-tagged MinE is 22.2 kDa.



## References for Supplemental Material

1. Ducat, T, Goto, NK (2010)  $^1\text{H}$ ,  $^{13}\text{C}$ ,  $^{15}\text{N}$  chemical shift assignments for the *Neisseria gonorrhoeae* MinE regulator of cell division septum placement. *Biomol NMR Assign* Submitted.
2. Delaglio, F, et al. (1995) NMRPipe: a multidimensional spectral processing system based on UNIX pipes. *J Biomol NMR* 6: 277-293.
3. Liang, B, Bushweller, JH, Tamm, LK (2006) Site-directed parallel spin-labeling and paramagnetic relaxation enhancement in structure determination of membrane proteins by solution NMR spectroscopy. *J Am Chem Soc* 128: 4389-4397.
4. Farrow, NA, et al. (1994) Backbone dynamics of a free and phosphopeptide-complexed Src homology 2 domain studied by  $^{15}\text{N}$  NMR relaxation. *Biochemistry* 33: 5984-6003.
5. Clore, MG, et al. (1990) Deviations from the simple two-parameter model-free approach to the interpretation of nitrogen-15 nuclear magnetic relaxation of proteins. *J Am Chem Soc* 112: 4989-4991.
6. Lipari, G, Szabo, A (1982a) Model-free approach to the interpretation of nuclear magnetic resonance relaxation in macromolecules. 1. Theory and range of validity. *J Am Chem Soc* 104: 4546-4559.
7. Lipari, G, Szabo, A (1982b) Model-free approach to the interpretation of nuclear magnetic resonance relaxation in macromolecules. 2. Analysis of experimental results. *J Am Chem Soc* 104: 4559-4570.
8. Dosset, P, Hus, JC, Blackledge, M, Marion, D (2000) Efficient analysis of macromolecular rotational diffusion from heteronuclear relaxation data. *J Biomol NMR* 16: 23-8.

9. Vriend, G (1990) WHAT IF: a molecular modeling and drug design program. *J Mol Graph* 8: 52-56.
10. Laskowski, RA, et al. (1996) AQUA and PROCHECK-NMR: programs for checking the quality of protein structures solved by NMR. *J Biomol NMR* 8: 477-486.
11. Battiste, JL, Wagner, G (2000) Utilization of site-directed spin labeling and high-resolution heteronuclear nuclear magnetic resonance for global fold determination of large proteins with limited nuclear overhauser effect data. *Biochemistry* 39: 5355-5365.
12. Koradi, R, Billeter, M, Wüthrich, K (1996) MOLMOL: a program for display and analysis of macromolecular structures. *J Mol Graph* 14: 51-55.
13. Larkin, MA, et al. (2007) Clustal W and Clustal X version 2.0. *Bioinformatics* 23: 2947-2948.

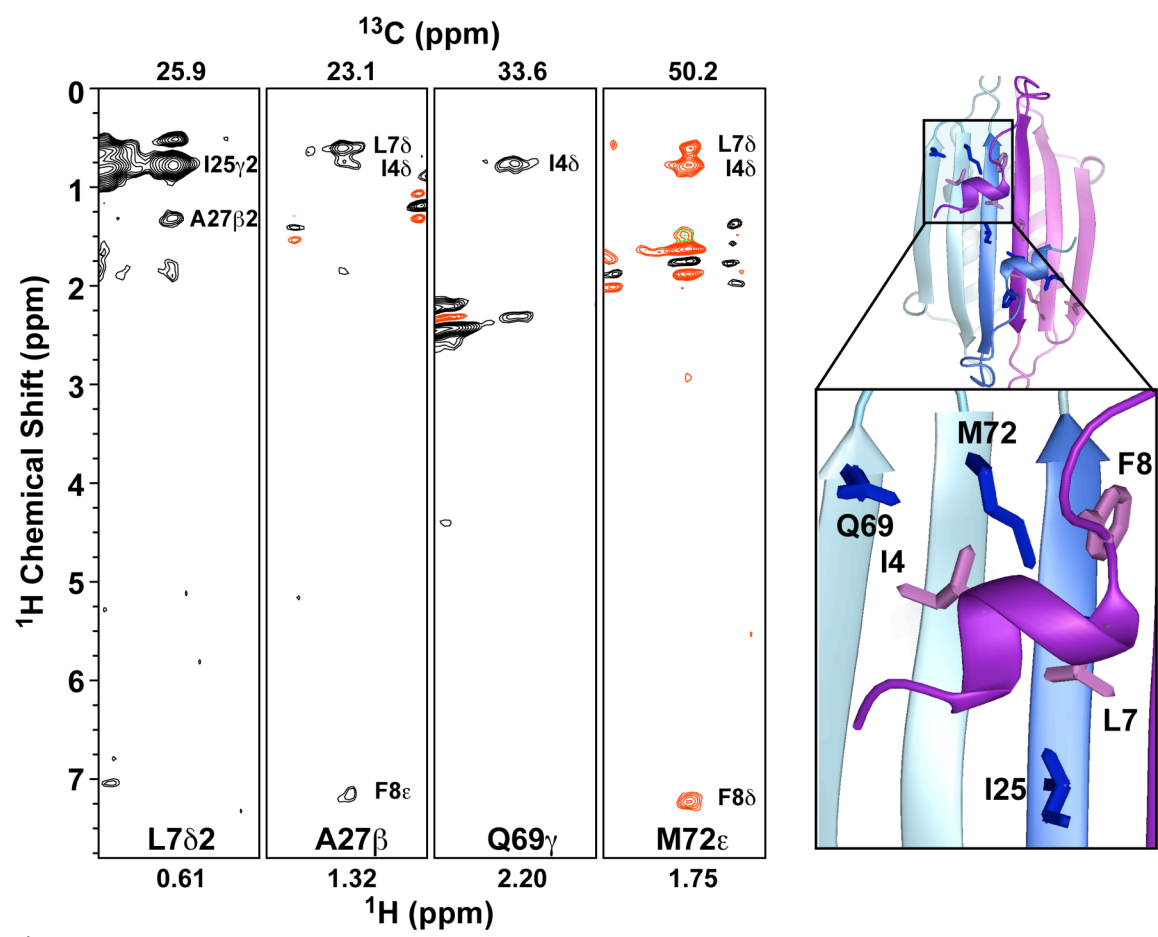


Figure S1

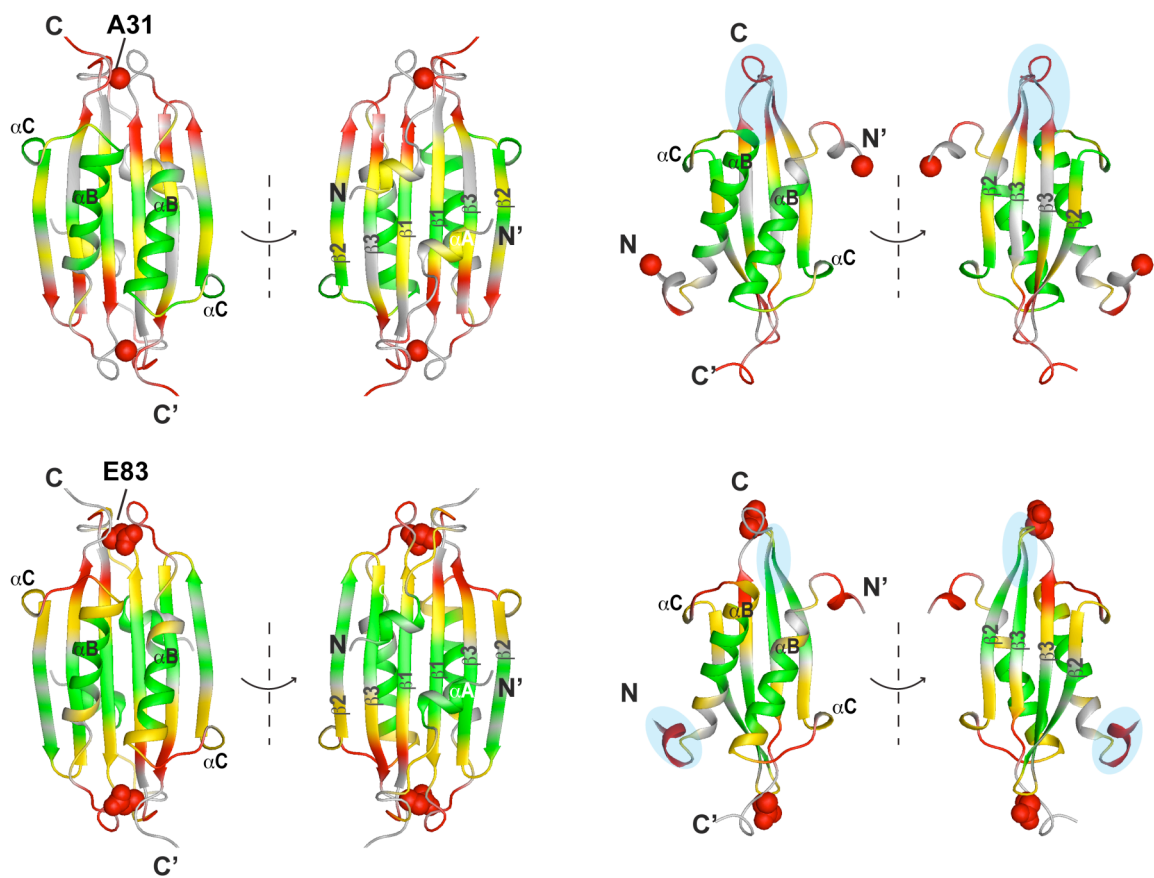


Figure S2

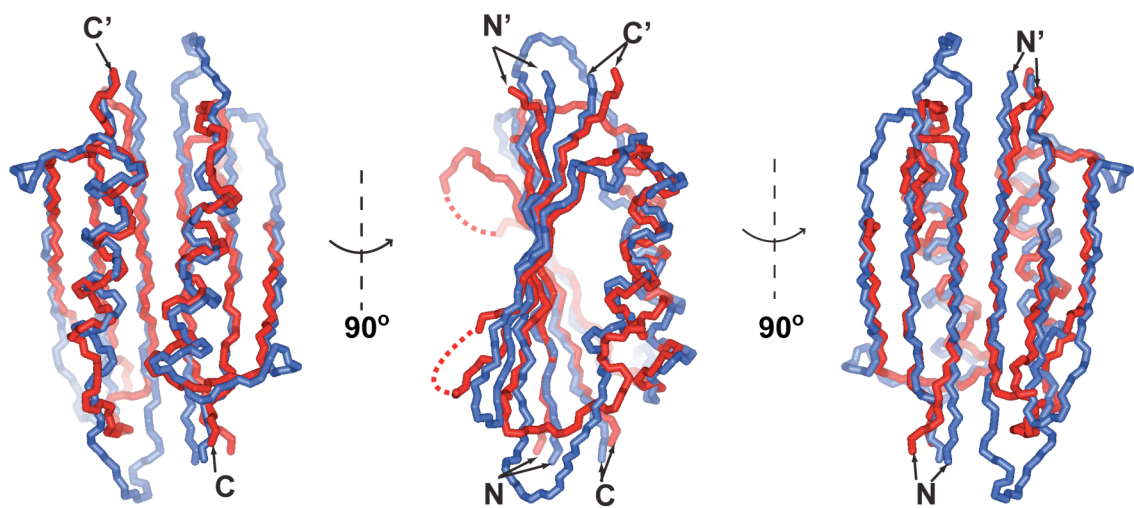


Figure S3

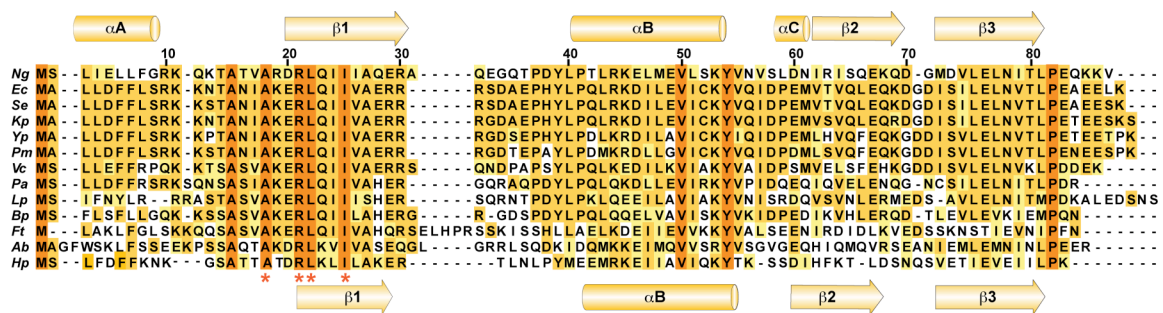


Figure S4

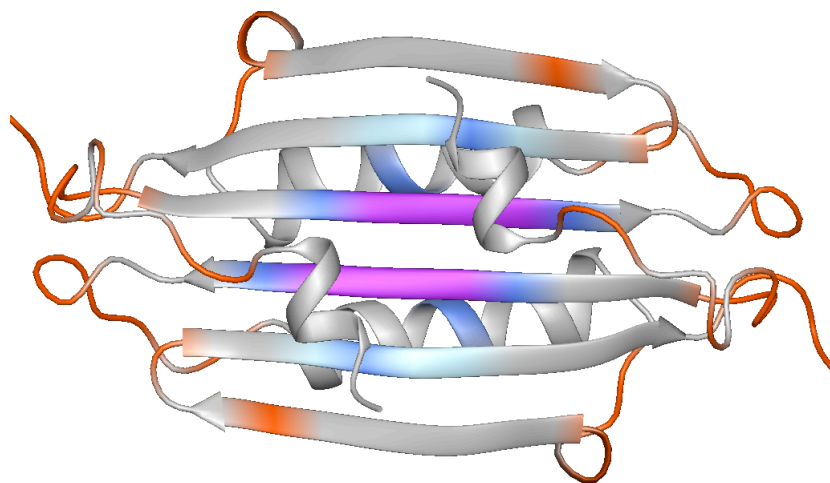


Figure S5

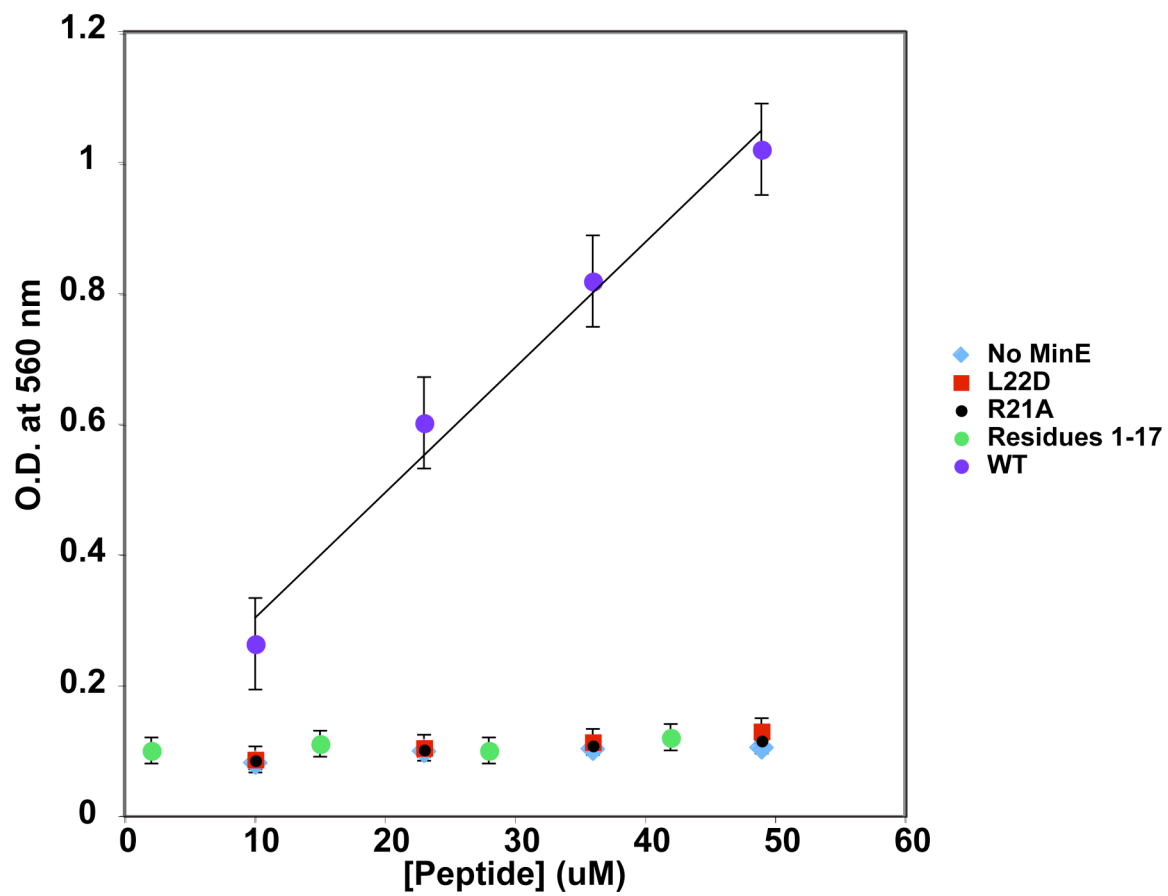


Figure S6

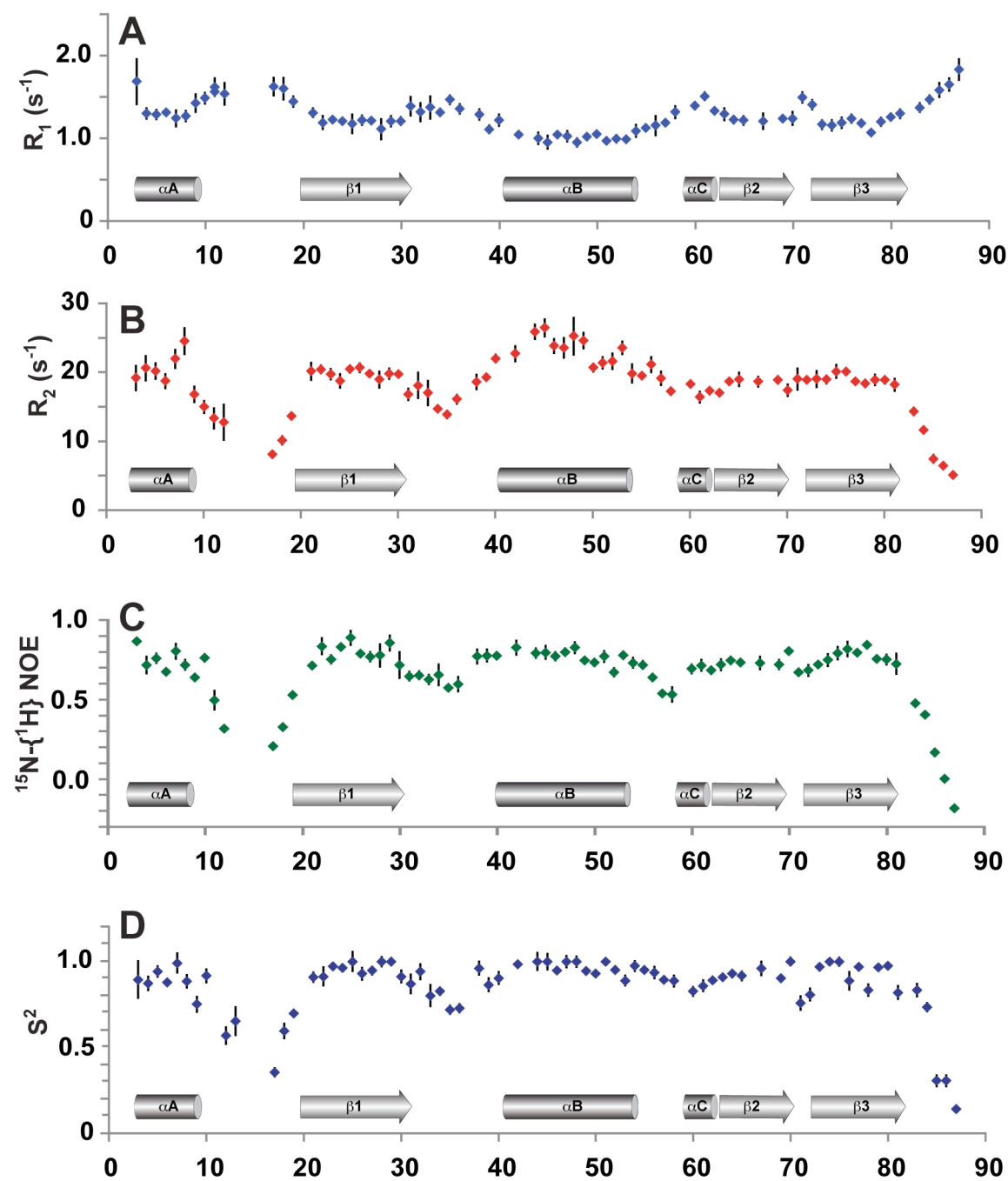


Figure S7

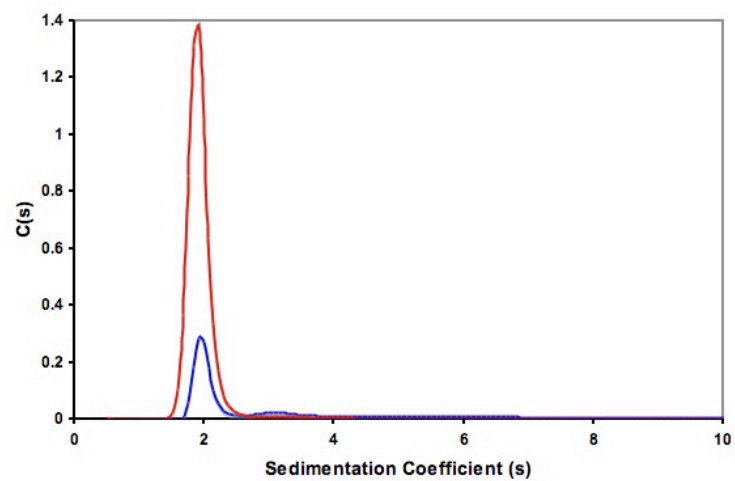


Figure S8